HHS Public Access

Author manuscript

Phys Med Biol. Author manuscript; available in PMC 2017 September 21.

Published in final edited form as:

Phys Med Biol. 2016 September 21; 61(18): 6668–6683. doi:10.1088/0031-9155/61/18/6668.

Anatomically-Aided PET Reconstruction Using the Kernel Method

Will Hutchcroft[1], **Guobao Wang**[1], **Kevin T. Chen**[2], **Ciprian Catana**[2], and **Jinyi Qi**[1]

Jinyi Qi: qi@ucdavis.edu

[1]Department of Biomedical Engineering, University of California-Davis, Davis, CA, USA

[2]Martinos Center for Biomedical Imaging, Department of Radiology, Massachusetts General Hospital and Harvard Medical School, Charlestown, MA, USA

Abstract

This paper extends the kernel method that was proposed previously for dynamic PET reconstruction, to incorporate anatomical side information into the PET reconstruction model. In contrast to existing methods that incorporate anatomical information using a penalized likelihood framework, the proposed method incorporates this information in the simpler maximum likelihood (ML) formulation and is amenable to ordered subsets. The new method also does not require any segmentation of the anatomical image to obtain edge information. We compare the kernel method with the Bowsher method for anatomically-aided PET image reconstruction through a simulated data set. Computer simulations demonstrate that the kernel method offers advantages over the Bowsher method in region of interest (ROI) quantification. Additionally the kernel method is applied to a 3D patient data set. The kernel method results in reduced noise at a matched contrast level compared with the conventional ML expectation maximization (EM) algorithm.

1. Introduction

Positron emission tomography (PET) is a primary tool in the detection and characterization of cancer, neurological disorders and cardiovascular disease (Peller *et al* 2012). By imaging the coincident annihilation photons from an injected radiotracer, PET allows for the acquisition of functional information for a wide range of biochemical and physiological processes. However, PET suffers from low spatial resolution due to detector blurring effects, positron range and photon non-colinearity. The limited photon count in PET data also requires spatial smoothing to reduce noise.

In contrast, anatomic imaging modalities such as computed tomography (CT) and magnetic resonance tomography (MRI) offer higher spatial resolution and accurate boundary information. As of 2006, more than 95% of PET systems sold were dual modality PET/CT systems (Townsend 2006) implying that the overwhelming majority of PET systems currently in use are as such. The benefit of PET/CT systems has been primarily through attenuation correction for PET and image coregistration; how best to further utilize anatomical information within PET reconstruction remains an open question. Moreover, a large body of recent work has been devoted to developing PET/MRI systems offering simultaneous data acquisition (Judenhofer *et al* 2008, Judenhofer *et al* 2007, Schwenzer *et al*

2012, Pichler *et al* 2010, Catana *et al* 2008, Catana *et al* 2012). Simultaneous data acquisition offers hardware-based image coregistration, reducing artifacts due to patient motion (Catana *et al* 2011) as well as enabling temporally correlated cross-modal data sets (Sander *et al* 2013).

Methods for incorporating anatomical information into PET image reconstruction have existed for some time now, e.g., (Leahy and Yan 1991, Fessler *et al* 1992, Comtat *et al* 2002, Bowsher *et al* 1996, Sastry and Carson 1997, Hero *et al* 1999, Rangarajan *et al* 2000, Baete *et al* 2004, Bataille *et al* 2006, Ouyang *et al* 1994, Lipinski *et al* 1997, Pramuthu and Hero 1998, Ardekani *et al* 1996, Alessio and Kinahan 2006, Dewaraja *et al* 2010, Tang and Rahmim 2009*b*, Tang and Rahmim 2009*a*, Cheng-Liao and Qi 2011, Somayajula *et al* 2011, Shidahara *et al* 2012, Nguyen and Lee 2013, Loeb *et al* 2015). The fact that MRI and CT are able to generate images with high resolution and SNR, two areas where PET images may be comparatively lacking, combined with the high correlation between PET tracer distributions and anatomically delineated regions, makes the pursuit a natural one. Most of the existing methods incorporate anatomical information through the penalized likelihood framework. One particularly successful example is the Bowsher method (Bowsher *et al* 2004) which computes the neighborhood of each pixel in an anatomically informed penalty function and does not require any segmentation. A recent work (Vunckx *et al* 2012) compared three algorithms for incorporating anatomical side information into PET reconstruction. The modified Bowsher method (Bowsher *et al* 2004, Vunckx *et al* 2010), was shown to offer superior quantitative accuracy when compared to post-smoothed maximum likelihood expectation maximization (ML EM) reconstruction, MAP reconstruction with a relative difference prior, and MAP reconstruction using an anatomy-specific joint entropy prior. The Bowsher method is used for comparison in the work presented here.

Wang and Qi proposed an alternative framework for incorporating side information into PET reconstruction based upon kernel methods from machine learning (Wang and Qi 2015). The kernel method has the advantage of simplicity in its implementation by using the popular ML EM algorithm. The original development of the kernel method was primarily focused on dynamic PET reconstruction where side information was obtained from temporal data. Here we extend the kernel method to anatomically-aided PET image reconstruction. Rather than using temporal features as in dynamic PET reconstruction, we employ patch-based MR image features to form the kernel matrix. We evaluated the kernel method using both computer simulation data and real patient data acquired on a brain PET/MR scanner.

2. Theory

2.1. Kernel Based Anatomically-Aided Reconstruction

PET data are commonly modeled as independent Poisson random variables with log likelihood,

$$L(\boldsymbol{y}|\overline{\boldsymbol{y}})=\sum_{i=1}^{M} y_i \log \overline{y}_i - \log \overline{y}_i \quad (1)$$

where the data vector $\boldsymbol{y}$ has expectation $\bar{\boldsymbol{y}}$. The expectation is a function of the image vector $\boldsymbol{x}$ through the following affine transform,

$$\bar{\boldsymbol{y}}=\boldsymbol{P}\boldsymbol{x}+\boldsymbol{r} \quad (2)$$

where $\boldsymbol{P} \in \mathbb{R}^{M\times N}$ is the system matrix with p_{ij} denoting the probability of detecting an event originating in voxel j in detector pair i, and $\boldsymbol{r}$ a vector encompassing random and scattered events. M and N represent the number of detector bins and voxels, respectively.

Many existing works on anatomically-aided PET image reconstruction have focused on incorporating anatomical information through the use of a penalty or prior function that encourages smoothness within anatomical regions while allowing sharp transition between anatomical regions (Bai *et al* 2013). Here we present a different approach that encodes anatomical information in the image representation by using the kernel trick. The basic idea is to represent the PET image $\boldsymbol{x}$ by a linear function of transformed anatomical features in a high-dimensional space. This can be accomplished by defining a kernel function on every pair of anatomical pixels j and k. The PET image at pixel j can then be written as (Wang and Qi 2015)

$$x_j=\sum_k \alpha_k \kappa(\boldsymbol{f}_j, \boldsymbol{f}_k), \quad (3)$$

where $\boldsymbol{f}_j$ and $\boldsymbol{f}_k$ are anatomical feature vectors for pixels j and k, respectively. In this work, each feature vector consists of pixel intensity values in a patch extracted from the high-resolution MR image. The vector $\boldsymbol{\alpha}$ is referred to as the coefficient image. There are a variety of choices of the kernel function κ. A common choice in many applications is the radial Gaussian kernel,

$$\kappa(\boldsymbol{f}_j, \boldsymbol{f}_k)=\exp\left(\frac{-\|\boldsymbol{f}_j-\boldsymbol{f}_k\|^2}{\sigma^2}\right) \quad (4)$$

where the parameter σ controls the edge sensitivity. Figure 1 depicts the kernel feature extraction process.

The above kernel representation can be written in a matrix-vector form as

$$\boldsymbol{x}=\boldsymbol{K}\boldsymbol{\alpha} \quad (5)$$

where the (j, k)th element of the kernel matrix $\boldsymbol{K}$ is equal to $\kappa(\boldsymbol{f}_j, \boldsymbol{f}_k)$. The column vectors of the kernel matrix $\boldsymbol{K}$ can also be viewed as a set of basis functions for the image representation. For computational efficiency, a k-nearest-neighbor (kNN) search is carried out for each pixel based on the Euclidean distance between $\boldsymbol{f}_k$ and $\boldsymbol{f}_j$. A search neighborhood, n_b, as well as number of neighbors, k, are specified beforehand. Only those pixels as

determined by the *k*NN search are allowed to contribute, resulting in the following definition,

$$K_{jk}=\begin{cases}\kappa(\boldsymbol{f}_j,\boldsymbol{f}_k), & f_k\in k\text{NN of } f_j,\\ 0, & \text{otherwise.}\end{cases} \quad (6)$$

This ensures that the kernel matrix $\boldsymbol{K}$ is sparse. For the purpose of reconstructing an image, we found that a large value of σ yielded more accurate results quantitatively, as determined by bias-variance analysis. Consequently, $\kappa(\boldsymbol{f}_j, \boldsymbol{f}_k)$ was set to 1 in this study. In order to ensure that the kernel transformation preserves counts, $\boldsymbol{K}$ is row normalized.

By substituting (5) into (2), the kernelized forward projection model is obtained

$$\overline{\boldsymbol{y}}=\boldsymbol{PK\alpha}+\boldsymbol{r}. \quad (7)$$

The optimization problem for image reconstruction then becomes

$$\hat{\boldsymbol{\alpha}}=\arg\max_{\boldsymbol{\alpha}\geq 0} L(\boldsymbol{y}|\boldsymbol{K\alpha}), \quad (8)$$

and may be solved by the well-known expectation-maximization (EM) algorithm. The update equation is

$$\boldsymbol{\alpha}^{n+1}=\frac{\boldsymbol{\alpha}^n}{\boldsymbol{K}^T\boldsymbol{P}^T\mathbf{1}}\left(\boldsymbol{K}^T\boldsymbol{P}^T\frac{\boldsymbol{y}}{\boldsymbol{PK\alpha}^n+\boldsymbol{r}}\right), \quad (9)$$

where the vector multiplication and division are performed element by element. The update equation share the same form as that was used in PET image reconstruction with supervoxels (Jiao *et al* 2015) by replacing the kernel matrix with the proper basis functions. Once the coefficient image estimate $\hat{\boldsymbol{\alpha}}$ is obtained, the final image estimate $\hat{\boldsymbol{x}}$ is given by

$$\hat{\boldsymbol{x}}=\boldsymbol{K}\hat{\boldsymbol{\alpha}}. \quad (10)$$

Comparison with inter-iteration nonlocal mean filtering—Equation (10) can be viewed as an anatomical based nonlocal mean (NLM) post-filtering operation. Naturally one may consider performing the NLM filtering inside the standard ML EM iteration, which would result in the following update equation:

$$\boldsymbol{\alpha}^{n+1}=\frac{\boldsymbol{K\alpha}^n}{\boldsymbol{P}^T\mathbf{1}}\left(\boldsymbol{P}^T\frac{\boldsymbol{y}}{\boldsymbol{PK\alpha}^n+\boldsymbol{r}}\right). \quad (11)$$

In comparison, the kernel method in (9) guarantees convergence to an ML solution, but the inter-iteration NLM filtering algorithm in (11) does not.

2.2. The Bowsher Method

For comparison, we implemented the Bowsher method, which incorporates anatomical information through a prior function. The Bowsher method was found to perform very well in a previous study (Vunckx *et al* 2012). With regard to feature extraction, the modified Bowsher method treats the anatomical image in a manner similar to the kernel method. The difference lies in how the information is further incorporated into image reconstruction. In the Bowsher method, the k-nearest neighbors of pixel *j* form the set $\mathcal{N}_j$ and a penalty function is defined as

$$U(\boldsymbol{x})=\sum_j \sum_{k\in\mathcal{N}_j(\boldsymbol{f})} (x_j - x_k)^2. \quad (12)$$

By specifying the penalty function this way, the inter-pixel smoothing is restricted to those pixels that are anatomically similar.

The PET image is estimated using the penalized likelihood framework

$$\hat{\boldsymbol{x}}=\arg\max_{\boldsymbol{x}\geq 0} L(\boldsymbol{y}|\overline{\boldsymbol{y}}=\boldsymbol{P}\boldsymbol{x}+\boldsymbol{r}) - \beta U(\boldsymbol{x}) \quad (13)$$

where β is the parameter that controls the strength of the regularization. We used De Pierro's algorithm (De Pierro 1995), which guarantees convergence to a global optimum, to find the penalized likelihood estimate.

3. Computer Simulations

3.1. Simulation Data

Computer simulation was performed to assess the performance of the proposed kernel method. A MRI data set was obtained from the BrainWeb project (Cocosco *et al* 1997) with 256×256 voxels in the axial plane and 1-mm isotropic voxel size. A suitable axial slice displaying regions of grey and white matter was chosen. The skull and cerebral spinal fluid were then removed using a region growing algorithm. To generate a simulated PET image, the remaining interior tissue was segmented into grey matter and white matter and resized to 128×128, with 2-mm pixels. Intensity values of 4 and 1 were assigned, respectively. A circular lesion with diameter of 5 pixels and intensity of 8 was then added to the grey matter in the PET image. In addition to the original MR image, another anatomical prior image was generated by adding a hypointense lesion with 1:2 contrast with regard to the surrounding tissue at the same location as that of the PET data. The lesion was smoothed using a Gaussian filter to avoid an artificially sharp boundary. Both MR prior images were then resized to 384×384 pixels so that each PET pixel corresponded to a 3×3 patch in the MR images. The prior image containing the lesion will be referred to as the lesion prior and the

unmodified MR prior as the lesion-less prior. Figure 2 shows the simulated PET image along with the two prior images.

For the simulation reconstructions, we modeled a GE Discovery ST PET/CT scanner in two-dimensional mode (Mawlawi *et al* 2004). Each detector ring of the scanner consists of 420 crystals. Each crystal face is 6.3 mm wide. The 2D sinogram contains 249 radial bins and 210 angular projections. The PET phantom image was forward projected using the system matrix to generate the noise-free projection data. A uniform sinogram with value equal to 20% of the mean of the noise-free sinogram was added to simulate background events (randoms and scatters). Finally, a set of 100 noisy realizations was generated by introducing poisson noise to the sinogram with the expected total number of events set to 500k.

3.2. Parameter Optimization

Images were reconstructed using the ML EM algorithm and the two anatomically-aided methods with a broad parameter range. In both methods, *k*NN search was performed in a local window for each pixel in the PET image. Four search window sizes were studied, with a variant number of included neighbors for each. The search window size, along with the corresponding number of neighbors, were: 3 × 3 window with 2 to 9 neighbors, 5 × 5 window with 4 to 24 neighbors, 7 × 7 window with 4 to 48 neighbors, 9 × 9 window with 5 to 80 neighbors.

3.3. Region of Interest Quantification

3.3.1. Bias-Variance Analysis—The lesion in the grey matter shown in Figure 2(a) was chosen as the region of interest (ROI). Standard deviation percentage vs. bias percentage curves were generated for each reconstruction. The mean ROI intensity of the *i*th realization, $\overline{x}^{i}_{\mathrm{ROI}}$, was first calculated and the mean ROI intensity was averaged over all noisy realizations as,

$$\overline{x}^{\mathrm{avg}}_{\mathrm{ROI}} = \sum_{k=1}^{n} \overline{x}^{i}_{\mathrm{ROI}}. \quad (14)$$

The bias percentage was calculated by,

$$\mathrm{Bias}\% = \frac{(\overline{x}^{\mathrm{avg}}_{\mathrm{ROI}} - \overline{x}^{\mathrm{true}}_{\mathrm{ROI}})}{\overline{x}^{\mathrm{true}}_{\mathrm{ROI}}} \times 100\%, \quad (15)$$

where $\overline{x}^{\mathrm{true}}_{\mathrm{ROI}}$ is the true ROI mean. The standard deviation percentage was calculated by,

$$\mathrm{SD}\% = \left(\frac{1}{\overline{x}^{\mathrm{true}}_{\mathrm{ROI}}} \sqrt{\frac{1}{n-1} \sum_{i=1}^{n} (\overline{x}^{i}_{\mathrm{ROI}} - \overline{x}^{\mathrm{avg}}_{\mathrm{ROI}})^2} \right) \times 100\%. \quad (16)$$

For the ML EM and kernel methods, the standard deviation percentage vs. bias percentage curves were plotted by varying iteration number from 30 to 300. For the Bowsher method, the curves were generated by varying the penalty parameter β and with a fixed iteration number of 300.

3.3.2. Lesion Contrast Recovery Coefficient—Lesion quantification was studied through the contrast recovery coefficient (CRC). For the *i*th realization, the CRC was calculated by

$$\mathrm{CRC}^i=(\frac{\overline{x}^i_{\mathrm{ROI}}}{\overline{x}^i_{\mathrm{BGD}}}-1)/(\frac{\overline{x}^{\mathrm{true}}_{\mathrm{ROI}}}{\overline{x}^{\mathrm{true}}_{\mathrm{BGD}}}-1), \quad (17)$$

where $\overline{x}^i_{\mathrm{BGD}}$ is the mean intensity of the background and $\overline{x}^{\mathrm{true}}_{\mathrm{BGD}}$ is the true background intensity. The CRC was averaged over realizations and plotted against its standard deviation to obtain a CRC vs. SD curve. As in ROI quantification, the ML EM and kernel method were controlled by iteration number, while the Bowsher method was regularized by β. For the Bowsher method, 300 iterations were used to ensure convergence. The background region was chosen in the white matter as shown in Figure 3.

3.4. Image Signal-to-Noise Ratio

In addition to the above methods in ROI quantification, overall image quality was assessed by the image signal-to-noise ratio (SNR) defined as,

$$\mathrm{SNR}=10\log_{10}(\frac{\|x_{\mathrm{recon}}\|^2}{\|x_{\mathrm{recon}}-x_{\mathrm{true}}\|^2}) \quad (18)$$

where ‖‖ denotes the Euclidean norm and x_{recon} and x_{true} are the reconstructed image and ground truth, respectively.

4. Simulation Results

4.1. Lesion Prior

4.1.1. Reconstructed Images—Figure 4 contains reconstructed images for all algorithms. For the Bowsher and kernel methods, four different search window sizes were investigated. The reconstruction parameters (iteration number for ML EM, iteration number and number of neighbors for the kernel method, and number of neighbors and β for the Bowsher method) were chosen to maximize the average image SNR. In all cases, β = 1 was found to give the best result with regard to SNR. Both anatomically aided methods show superior overall image quality and SNR to that of the ML EM algorithm. The Bowsher method was shown to yield slightly higher image SNR than the kernel method for a given search window size.

4.1.2. Bias-Variance Analysis—Bias percentage and standard deviation percentage were calculated as described in section IV D. Figure 5 shows performance plots for all neighborhood sizes. In each case, the number of neighbors were selected to achieve the best performance. Both anatomically aided methods give better bias-variance performance than the ML EM algorithm. In comparison, the kernel method achieved lower variance at a given bias level than the Bowsher method for all neighborhood sizes. The curved, oscillatory shape seen in the curves for the kernel method is representative of pixel coupling within the reconstruction. By tracking the intensity values of individual pixels through many iterations, it was seen that pixels within and just outside of the lesion display dampened oscillations that are of a similar frequency but out of phase with one another as the intensity values converge to a final value.

4.1.3. Contrast Recovery—Figure 6 displays the CRC vs. standard deviation curves for all three methods. As was done for the ROI quantification, the curves displayed for each window size correspond to the number of neighbors that yields the best performance for each. All methods yield similar performance in terms of CRC value, as expected. Both the kernel and Bowsher methods demonstrate improved performance over the ML EM algorithm.

4.2. Lesion-less Prior

In this section, anatomically aided images were reconstructed using the lesion-less prior image. It is expected that ROI quantification performance may suffer when no information on the ROI is included in the prior image. This case presents an interesting and realistic challenge. For all but the smallest search window size (3×3), this task proves too difficult for both the kernel and Bowsher methods. Larger window sizes yield poor performance when compared to the ML EM algorithm for both ROI quantification metrics. This result is expected as there is no information in the prior image to distinguish the lesion from its surrounding tissue and a large search window results in more erroneous coupling between pixels outside and inside the lesion. In this case, a smaller neighborhood size decreases the rate of such occurrence. In practice, a user would need to tailor the neighborhood size and number of chosen neighbors to select the desired level of anatomical influence. If a high level of confidence in correspondence between anatomical and functional information exists, then a larger neighborhood and number of neighbors will yield better performance. Figure 7 displays the best quantification performance for each algorithm. For the hot-lesion ROI quantification, the kernel method is able to achieve a reduction in noise compared to the EM algorithm. In the case of CRC vs. SD, the kernel method shows performance that closely mirrors that of the ML EM algorithm, while the Bowsher method shows slightly higher noise for CRC values between 0.7 and 0.9. For both methods of quantification, the use of all neighbors in the Bowsher method yields the best performance. For this level of inclusivity, the method gives no anatomically specific smoothing and is reduced to the standard penalized likelihood reconstruction with a quadratic penalty.

Figure 8 shows sampled reconstructed images at a matched bias level of the lesion ROI. The reconstructed hot lesions appear similar in all three images. The fact that the grey and white matter in the Bowsher reconstruction appears noisier than the EM reconstruction is because

noise is more uniform spatially in penalized maximum likelihood reconstruction (Qi and Leahy 1999), whereas it is more proportional to the image intensity in EM-based methods (Barrett *et al* 1994). If we were to compare images at a matched bias level of a cold region, a Bowsher reconstruction would appear less noisy than a EM reconstruction.

5. Clinical Patient Data

To further validate the kernel method, the algorithm was applied to a clinical patient data set acquired on a Siemens BrainPET insert operating inside the Siemens MAGNETOM 3-T MRI scanner. The PET insert consists of 32 detector cassettes, each consisting of 6 detector blocks. Each individual detector block is composed of a 12×12 array of lutetium oxyorthosilicate crystals (2.5×2.5×20 mm). Magnetic field insensitive avalanche photodiodes are used for readout purposes. For data processing, raw PET data was rebinned into the sinogram space using span 9 compression and a maximum ring difference of 67, resulting in a total of 1,399 sinograms. The sinogram dimensions are 192 angular projections and 256 radial bins. The tracer used was ^{18}F-FDG.

The clinical patient data was reconstructed using both the kernel method and ML EM, with 300 iterations for each. Correction factors for randoms, scatters, attenuation and detector normalization were estimated using the standard software provided by the manufacturer and included in the forward model in both reconstructions (Byars *et al* 2005, Watson 2000, Izquierdo-Garcia *et al* 2014). Figures 9 and 10 show coronal and axial images, respectively, for the two methods at iteration 50.

For quantitative comparison, we used the volume segmentations derived by FreeSurfer to define 3D ROI's. The white matter region in the left hemisphere was eroded to serve as the background region. Two regions of clinical interest, the hippocampus and the caudate, were used as targets of interest. These regions are displayed in Figure 11. Only one transaxial slice is shown for each region, but all the regions were defined in 3D.

The background noise was computed as the standard deviation of the white matter region, normalized by its mean activity. Similarly, mean contrast was computed within the target regions and normalized by the background mean. Quantification curves were generated by plotting these metrics over iteration and are shown in Figure 12. In comparison, the kernel method results in a 53% and 26% reduction in noise at a matched contrast level (95% of the maximum contrast achieved by ML EM) compared to the ML EM algorithm, in the caudate and hippocampus, respectively.

6. Conclusion

We proposed a kernel method to incorporate anatomical information in PET reconstruction. The computer simulation study showed that the kernel method can achieve better ROI quantification performance when compared to the ML EM algorithm, as well as the Bowsher method that utilizes the same anatomical information. The kernel method was also applied to real patient data acquired on a brain PET/MR scanner. The results showed that the kernel method achieves a significant reduction in noise at matched contrast, when compared to the ML EM algorithm.

While our work considers the case of features present in the PET data yet missing from the anatomical prior, other types of signal mismatch will likely exist in certain imaging scenarios. As an example, non-concurrent PET/MRI acquisition presents an increased likelihood of boundary mismatch between the two datasets. Under these conditions, care must be taken to maximize alignment between PET and MRI boundaries before applying an anatomically informed reconstruction. This will be addressed in the future work.

Acknowledgments

The authors would like to thank the anonymous reviewers for their insightful comments and suggestions. This work is supported by the National Institutes of Health under grant number R01EB014894 and R01EB000194. KT Chen is supported by Department of Defense (DoD) through the National Defense Science and Engineering Graduate Fellowship (NDSEG) Program.

References

Alessio AM, Kinahan PE. Improved quantitation for PET/CT image reconstruction with system modeling and anatomical priors. Medical Physics. 2006; 33(11):4095–4103. [PubMed: 17153389]

Ardekani BA, Braun M, Hutton BF, Kanno I, Iida H. Minimum cross-entropy reconstruction of PET images using prior anatomical information. Physics in Medicine and Biology. 1996; 41(11):2497–2517. [PubMed: 8938041]

Baete K, Nuyts J, Van Paesschen W, Suetens P, Dupont P. Anatomical-based FDG-PET reconstruction for the detection of hypo-metabolic regions in epilepsy. IEEE Transactions on Medical Imaging. 2004; 23(4):510–519. [PubMed: 15084076]

Bai B, Li Q, Leahy RM. Magnetic resonance-guided positron emission tomography image reconstruction. Semin Nucl Med. 2013; 43(1):30–44. [PubMed: 23178087]

Barrett HH, Wilson DW, Tsui BMW. Noise properties of the EM algorithm: I. Theory. Physics in Medicine and Biology. 1994; 39:833–846. [PubMed: 15552088]

Bataille F, Comtat C, Jan S, Sureau FC, Trebossen R. Brain PET partial-volume compensation using blurred anatomical labels. Nuclear Science Symposium Conference Record. 2006; 3:1817–1824.

Bowsher JE, Johnson VE, Turkington TG, Jaszczak RJCEJF, Coleman RE. Bayesian reconstruction and use of anatomical a priori information for emission tomography. IEEE Transactions on Medical Imaging. 1996; 15(5):673–686. [PubMed: 18215949]

Bowsher JE, Yuan H, Hedlund LW, Turkington TG, Akabani G, Badea A, Kurylo WC, Wheeler CT, Cofer GP, Dewhirst MW, Johnson GA. Utilizing MRI Information to Estimate F18-FDG Distributions in Rat Flank Tumors. IEEE Nuclear Science Symposium Conference Record. 2004; 00:2488–2492.

Byars L, Sibomana M, Burbar Z, Jones J, Panin V, Barker W, Liow JS, Carson R, Michel C. Variance reduction on randoms from coincidence histograms for the hrrt. Nuclear Science Symposium Conference Record, 2005 IEEE. 2005; 5:2622–2626.

Catana C, Benner T, van der Kouwe A, Byars L, Hamm M, Chonde DB, Michel CJ, El Fakhri G, Schmand M, Sorensen AG. MRI-assisted PET motion correction for neurologic studies in an integrated MR-PET scanner. J. Nucl. Med. 2011; 52(1):154–161. [PubMed: 21189415]

Catana C, Drzezga A, Heiss WD, Rosen BR. PET/MRI for neurological applications. Journal of nuclear medicine. 2012; 53(12):1916–1925. [PubMed: 23143086]

Catana C, Procissi D, Wu Y, Judenhofer MS, Qi J, Pichler BJ, Jacobs RE, Cherry SR. Simultaneous in vivo positron emission tomography and magnetic resonance imaging. Proc. Natl. Acad. Sci. U.S.A. 2008; 105(10):3705–3710. [PubMed: 18319342]

Cheng-Liao J, Qi J. PET image reconstruction with anatomical edge guided level set prior. Phys Med Biol. 2011; 56(21):6899–6918. [PubMed: 21983558]

Cocosco CA, Kollokian V, Kwan RKS, Evans AC. BrainWeb: Online interface to a 3D MRI simulated brain database. NeuroImage. 1997; 5(4):S425.

Comtat C, Kinahan PE, Fessler JA, Beyer T, Townsend DW, Defrise M, Michel C. Clinically feasible reconstruction of 3D whole-body PET/CT data using blurred anatomical labels. Physics in Medicine and Biology. 2002; 47:1–20. [PubMed: 11814220]

De Pierro A. A Modified Expectation Maximization Algorithm for Penalized Likelihood Estimation in Emission Tomography. IEEE Transactions on Medical Imaging. 1995; 14(1):132–137. [PubMed: 18215817]

Dewaraja YK, Koral KF, Fessler JA. Regularized reconstruction in quantitative SPECT using CT side information from hybrid imaging. Physics in Medicine and Biology. 2010; 55(9):2523–2539. [PubMed: 20393233]

Fessler JA, Clinthorne NH, Rogers WL. Regularized emission image reconstruction using imperfect side information. IEEE Transactions on Nuclear Science. 1992; 39(5):1464–1471.

Hero AO, Piramuthu R, Fessler JA, Titus SR. Minimax emission computed tomography using high-resolution anatomical side information and B-spline models. IEEE Transactions on Information Theory. 1999; 45(3):920–938.

Izquierdo-Garcia D, Hansen AE, Forster S, Benoit D, Schachoff S, Furst S, Chen KT, Chonde DB, Catana C. An SPM8-based approach for attenuation correction combining segmentation and nonrigid template formation: application to simultaneous PET/MR brain imaging. J. Nucl. Med. 2014; 55(11):1825–1830. [PubMed: 25278515]

Jiao J, Pawel M, Burgos N, Atkinson D, Hutton B, Arridge S, Ourselin S. Detail-preserving PET reconstruction with sparse image representation and anatomical priors. Inf Process Med Imaging. 2015; 24:540–551. [PubMed: 26221701]

Judenhofer MS, Catana C, Swann BK, Siegel SB, Cherry SR, Claussen CD, Pichler BJ. PET / MR Images Acquired with a Detector in a 7-T Magnet. Radiology. 2007; 244(3):807–814. [PubMed: 17709830]

Judenhofer MS, Wehrl HF, Newport DF, Catana C, Siegel SB, Becker M, Thielscher A, Kneilling M, Lichy MP, Eichner M, Klingel K, Reischl G, Widmaier S, Röcken M, Nutt RE, Machulla HJ, Uludag K, Cherry SR, Claussen CD, Pichler BJ. Simultaneous PET-MRI: a new approach for functional and morphological imaging. Nature medicine. 2008; 14(4):459–465.

Leahy, R.; Yan, X. ‘Lecture notes in computer science’ Information Processing in Medical Imaging. Springer; 1991. Incorporation of anatomical MR data for improved functional imaging with PET.

Lipinski B, Herzog H, Rota Kops E, Oberschelp W, Muller-Gartner HW. Expectation maximization reconstruction of positron emission tomography images using anatomical magnetic resonance information. IEEE Transactions on Medical Imaging. 1997; 16(2):129–136. [PubMed: 9101322]

Loeb R, Navab N, Ziegler SI. Direct parametric reconstruction using anatomical regularization for simultaneous PET/MRI data. IEEE Trans Med Imaging. 2015; 34(11):2233–2247. [PubMed: 25935030]

Mawlawi O, Podoloff Da, Kohlmyer S, Williams JJ, Stearns CW, Culp RF, Macapinlac H. Performance characteristics of a newly developed PET/CT scanner using NEMA standards in 2D and 3D modes. Journal of nuclear medicine : official publication, Society of Nuclear Medicine. 2004; 45(10):1734–1742.

Nguyen VG, Lee SJ. Incorporating anatomical side information into PET reconstruction using nonlocal regularization. IEEE Trans Image Process. 2013; 22(10):3961–3973. [PubMed: 23744678]

Ouyang X, Wong WH, Johnson VE, Xiaoping H, Chen C. Incorporation of correlated structural images in PET image reconstruction. IEEE Transactions on Medical Imaging. 1994; 13(4):627–640. [PubMed: 18218541]

Peller, P.; Subramaniam, R.; Guermazi, A. PET-CT and PET-MRI in Oncology. Springer; 2012.

Pichler BJ, Kolb A, Nägele T, Schlemmer HP. PET/MRI: paving the way for the next generation of clinical multimodality imaging applications. Journal of nuclear medicine : official publication, Society of Nuclear Medicine. 2010; 51(3):333–336.

Pramuthu R, Hero AO. Penalized maximum likelihood image reconstruction with min-max incorporation of noisy side information. IEEE International Conference on Acoustics, Speech, and Signal Processing. 1998; 5:2865–2868.

Qi J, Leahy RM. A Theoretical Study of the Contrast Recovery and Variance of MAP Reconstructions From PET data. IEEE Transactions on Medical Imaging. 1999; 18(4):293–305. [PubMed: 10385287]

Rangarajan A, Hsiao I, Gindi G. A Bayesian joint mixture framework for the integration of anatomical information in functional image reconstruction. Journal of Mathematical Imaging and Vision. 2000; 12(3):199–217.

Sander CY, Hooker JM, Catana C, Normandin MD, Alpert NM, Knudsen GM, Vanduffel W, Rosen BR, Mandeville JB. Neurovascular coupling to D2/D3 dopamine receptor occupancy using simultaneous PET/functional MRI. Proc. Natl. Acad. Sci. U.S.A. 2013; 110(27):11169–11174. [PubMed: 23723346]

Sastry S, Carson RE. Multimodality Bayesian algorithm for image reconstruction in positron emission tomography: a tissue composition model. IEEE Transactions on Medical Imaging. 1997; 16(6): 750–761. [PubMed: 9533576]

Schwenzer NF, Stegger L, Bisdas S, Schraml C, Kolb a, Boss a, Müller M, Reimold M, Ernemann U, Claussen CD, Pfannenberg C, Schmidt H. Simultaneous PET/MR imaging in a human brain PET/MR system in 50 patients–current state of image quality. European journal of radiology. 2012; 81(11):3472–3478. [PubMed: 22260898]

Shidahara M, Tsoumpas C, McGinnity CJ, Kato T, Tamura H, Hammers A, Watabe H, Turkheimer FE. Wavelet-based resolution recovery using an anatomical prior provides quantitative recovery for human population phantom PET [^{11}C]raclopride data. Phys Med Biol. 2012; 57(10):3107–3122. [PubMed: 22547469]

Somayajula S, Panagiotou C, Rangarajan A, Li Q, Arridge SR, Leahy RM. PET image reconstruction using information theoretic anatomical priors. IEEE Trans Med Imaging. 2011; 30(3):537–549. [PubMed: 20851790]

Tang, J.; Rahmim, A. Anatomy assisted MAP-EM PET image reconstruction incorporating joint entropies of wavelet subband image pairs; Nuclear Science Symposium Conference Record (NSS/MIC), 2009 IEEE; 2009a. p. 3741-3745.

Tang J, Rahmim A. Bayesian PET image reconstruction incorporating anato-functional joint entropy. Physics in Medicine and Biology. 2009b; 54(23):7063–7075. [PubMed: 19904028]

Townsend, D. Basic Science of PET and PET/CT. London: Springer; 2006.

Vunckx K, Atre A, Baete K, Reilhac A, Deroose CM, Laere KV, Nuyts J. Evaluation of Three MRI-Based Anatomical Priors for Quantitative PET Brain Imaging. IEEE Transactions on Medical Imaging. 2012; 31(3):599–612. [PubMed: 22049363]

Vunckx, K.; Nuyts, J.; Medicine, N.; Leuven, KU.; Leuven, B. Heuristic Modification of an Anatomical Markov Prior Improves its Performance; IEEE Nuclear Science Symposium Conference Record; 2010. p. 3262-3266.

Wang G, Qi J. PET image reconstruction using kernel method. IEEE Transactions on Medical Imaging. 2015; 34(1):61–71. [PubMed: 25095249]

Watson C. New, faster, image-based scatter correction for 3D PET. Nuclear Science, IEEE Transactions on. 2000; 47(4):1587–1594.

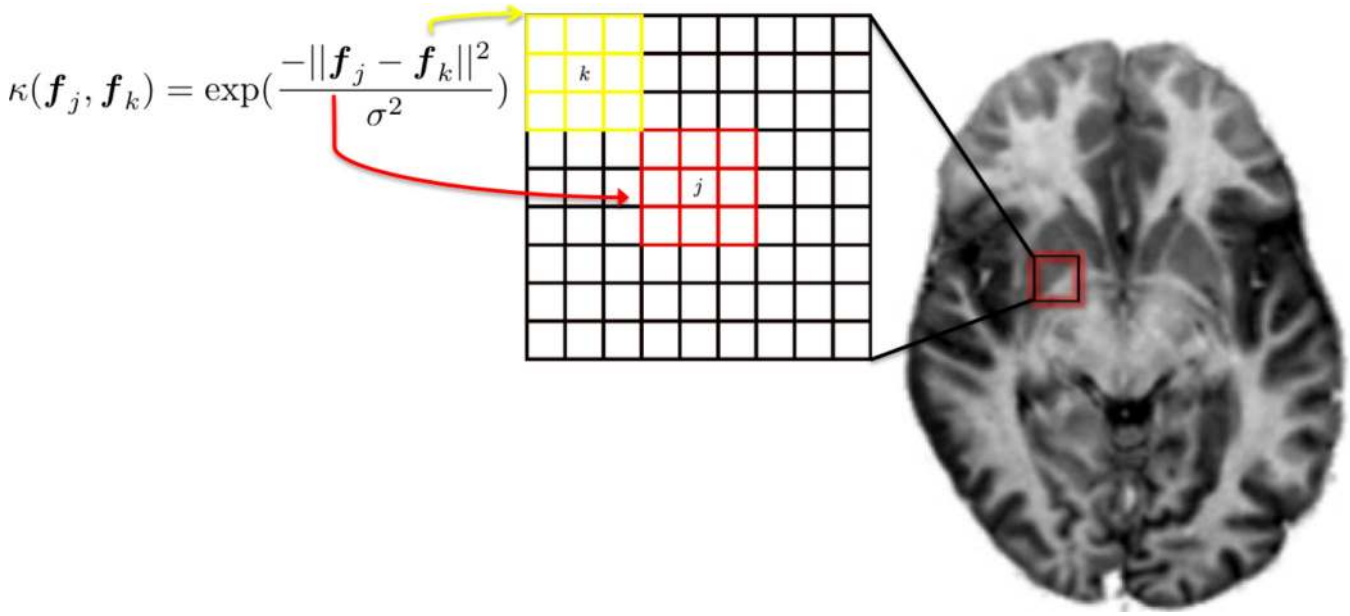

Figure 1.
Kernel feature extraction. The radial Gaussian kernel function computes the patch-wise similarity between two voxels in the anatomical image.

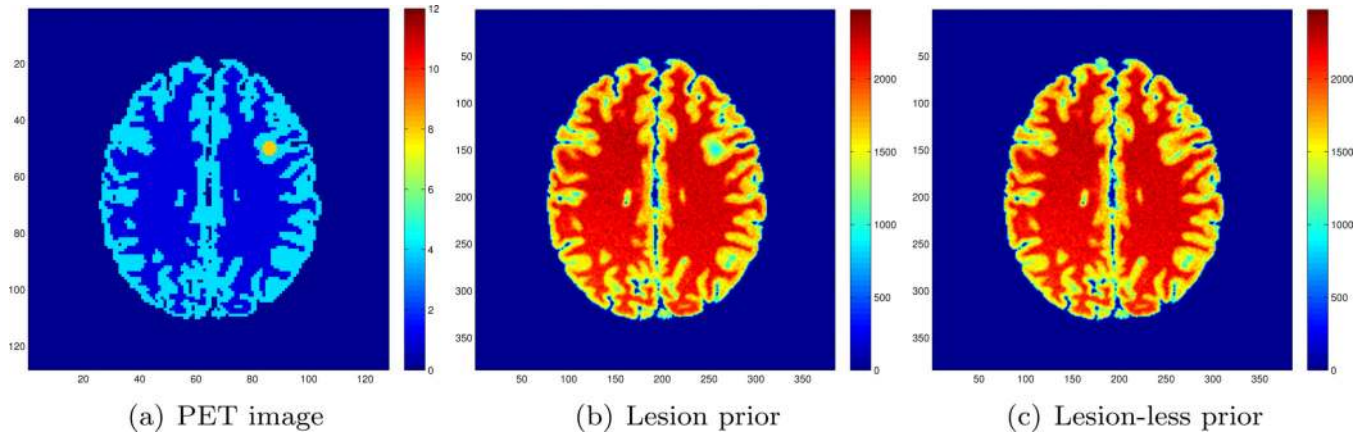

Figure 2.
PET image and MR image priors used for computer simulations.

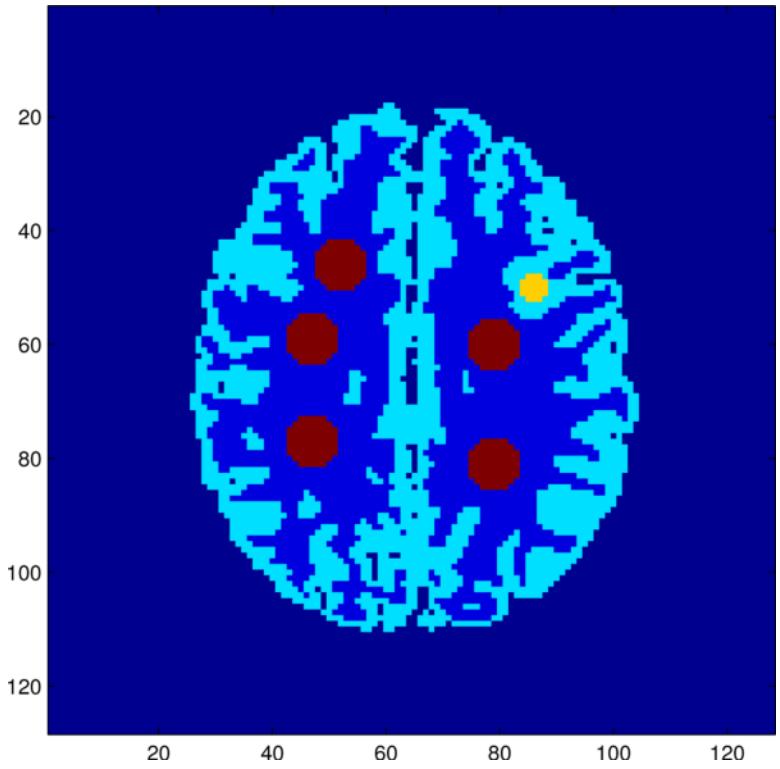

Figure 3.
The chosen lesion ROI (yellow) and background regions (red) for the CRC calculation.

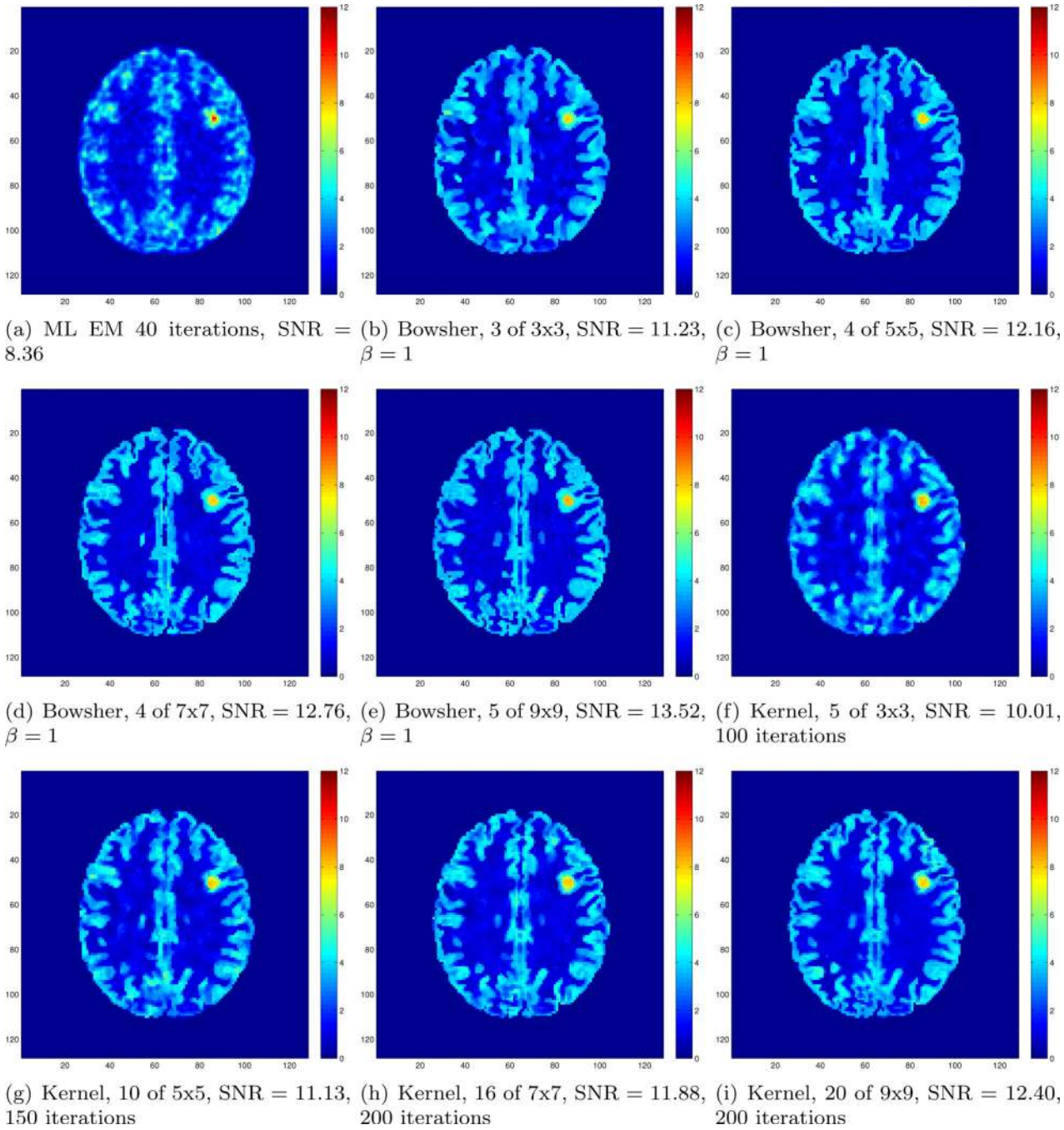

(a) ML EM 40 iterations, SNR = 8.36 (b) Bowsher, 3 of 3x3, SNR = 11.23, $\beta = 1$ (c) Bowsher, 4 of 5x5, SNR = 12.16, $\beta = 1$

(d) Bowsher, 4 of 7x7, SNR = 12.76, $\beta = 1$ (e) Bowsher, 5 of 9x9, SNR = 13.52, $\beta = 1$ (f) Kernel, 5 of 3x3, SNR = 10.01, 100 iterations

(g) Kernel, 10 of 5x5, SNR = 11.13, 150 iterations (h) Kernel, 16 of 7x7, SNR = 11.88, 200 iterations (i) Kernel, 20 of 9x9, SNR = 12.40, 200 iterations

Figure 4.

Reconstructed images of the simulated data. The number of iterations (EM and kernel methods) and the number of neighbors (Bowsher and kernel methods) were selected to yield the highest average image SNR. The anatomically-aided reconstructions displayed here used the lesion prior.

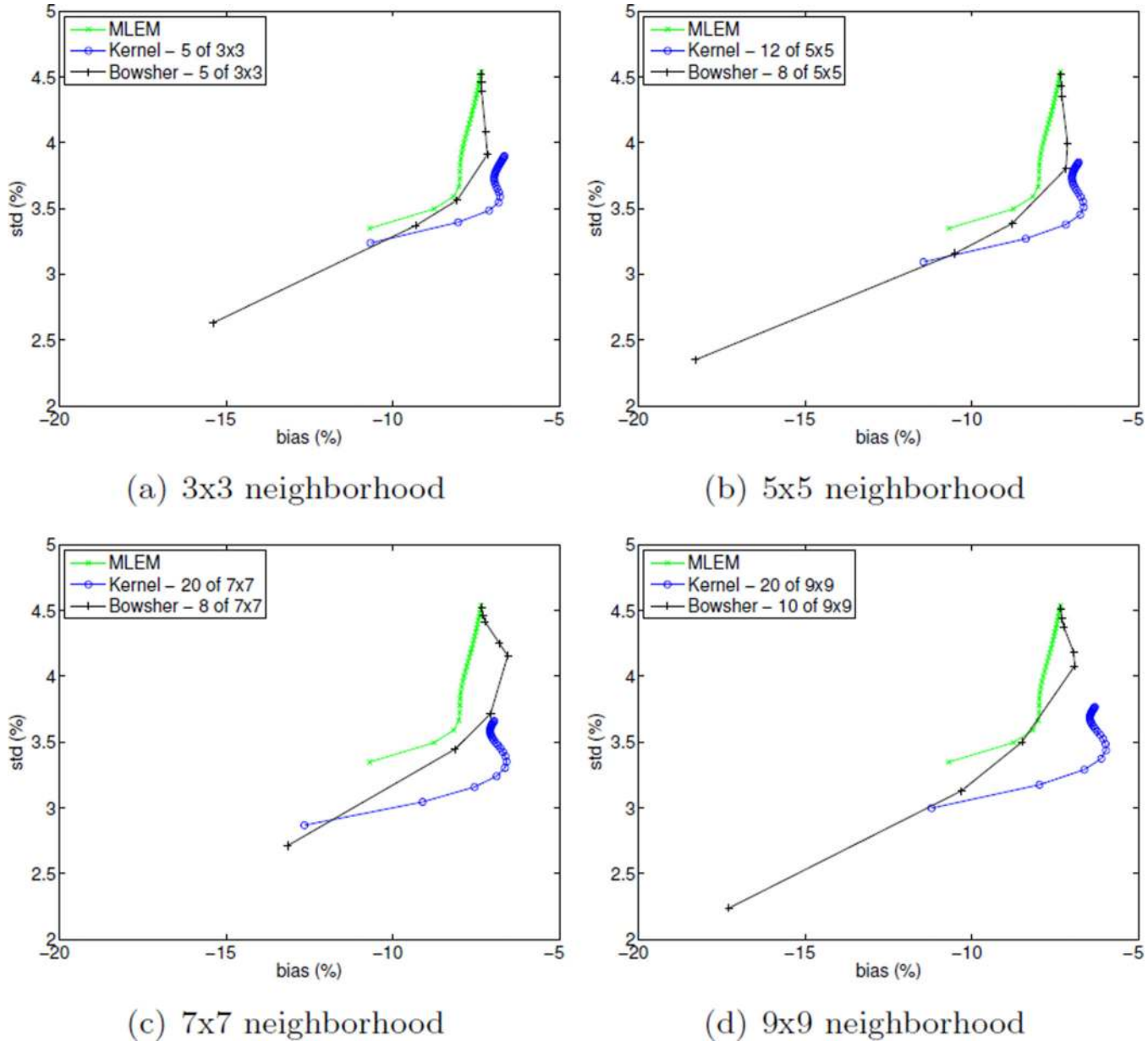

Figure 5.

Bias-variance trade-off curves for each neighborhood size. For both anatomical methods and for a given neighborhood size, the number of neighbors yielding the best bias-variance performance is shown. The anatomically-aided reconstructions used the lesion prior.

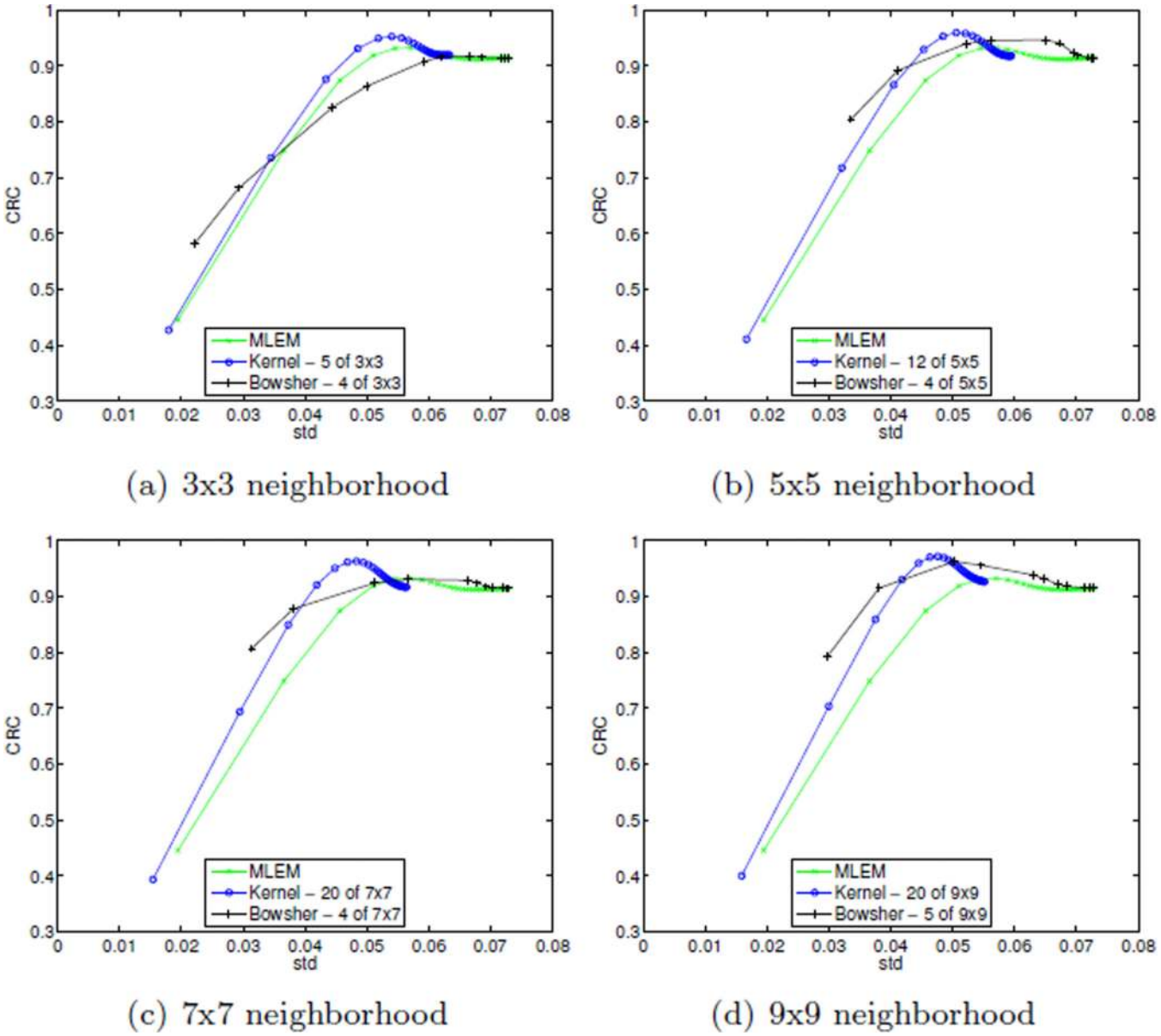

Figure 6.

CRC-SD trade-off curves for each neighborhood size. For both anatomical methods and for a given neighborhood size, the number of neighbors yielding the best CRC-SD performance is shown. The anatomically-aided reconstructions used the lesion prior.

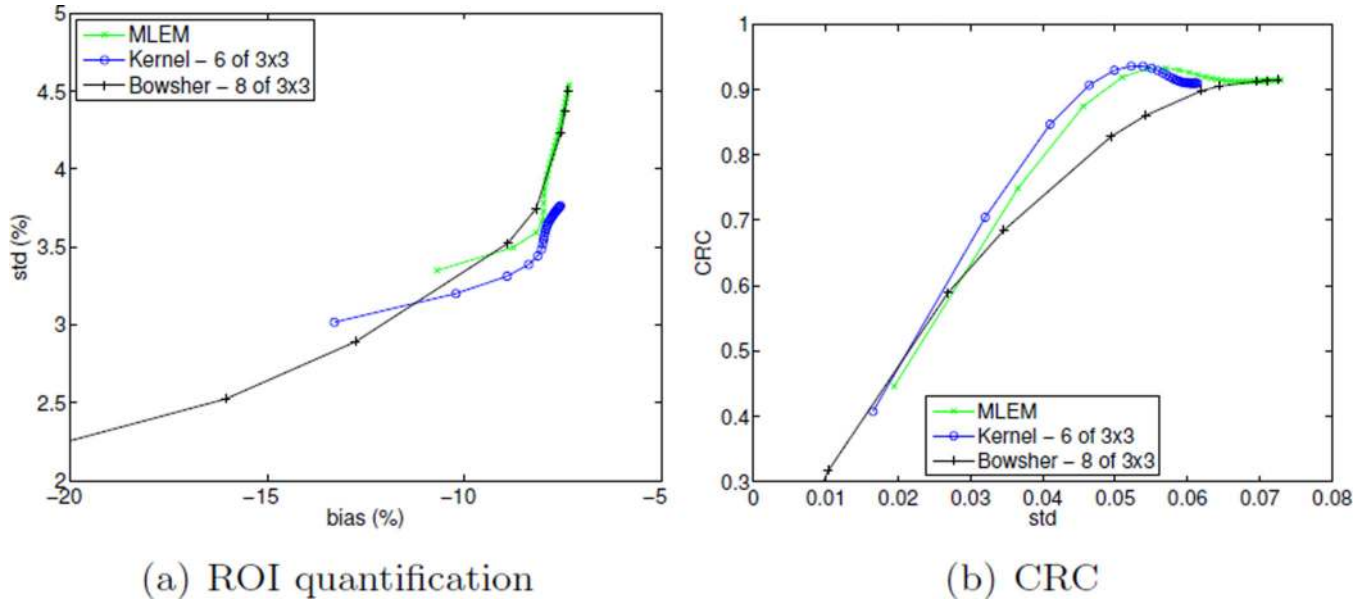

Figure 7.

ROI quantification performance given the lesion-less prior. Curves of the best performance are shown for each algorithm. (a) Bias-variance plot. (b) CRC-SD plot.

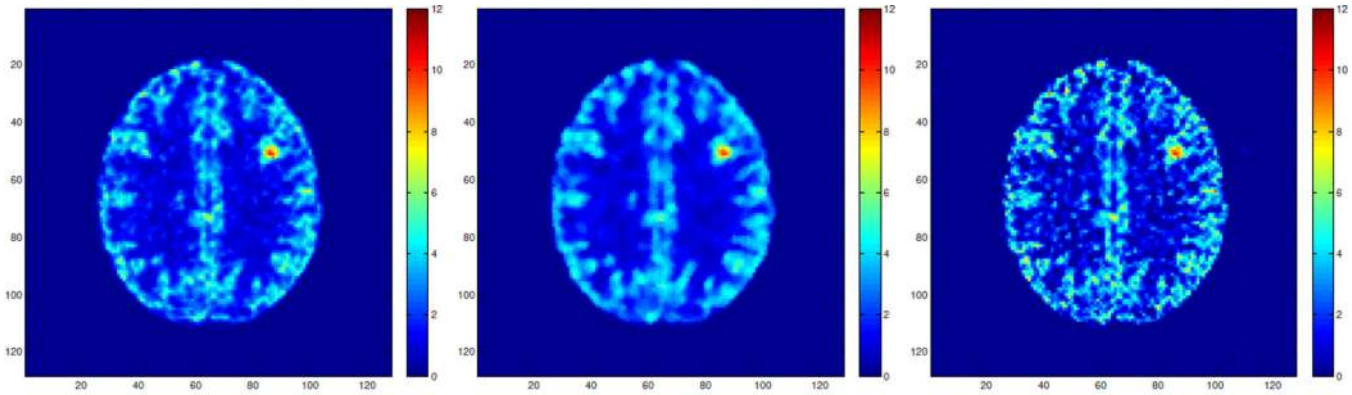

Figure 8.

Sample reconstructions at a fixed bias $\simeq -8.2\%$ for the lesion ROI quantification. Anatomically aided reconstructions were generated using the lesion-less prior.

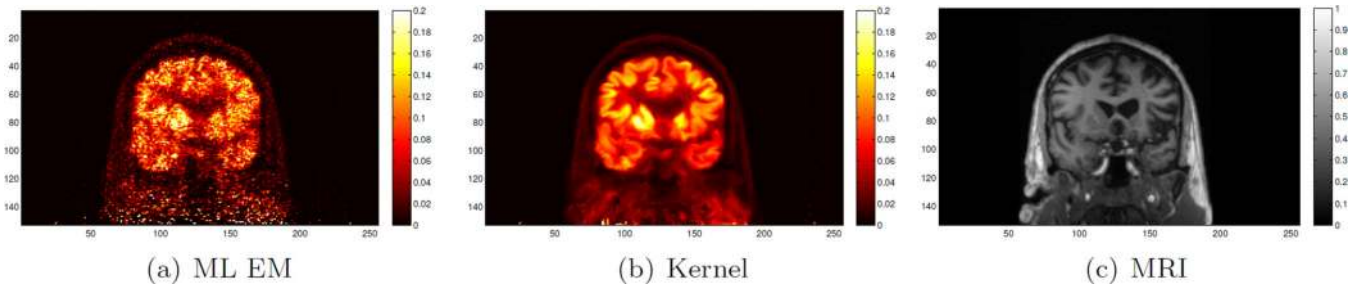

Figure 9.

A coronal slice of the reconstructed patient images. (a) ML EM reconstruction with 50 iterations. (b) The kernel method with 40 neighbors from a $7 \times 7 \times 7$ search window. (c) MR image of the same slice.

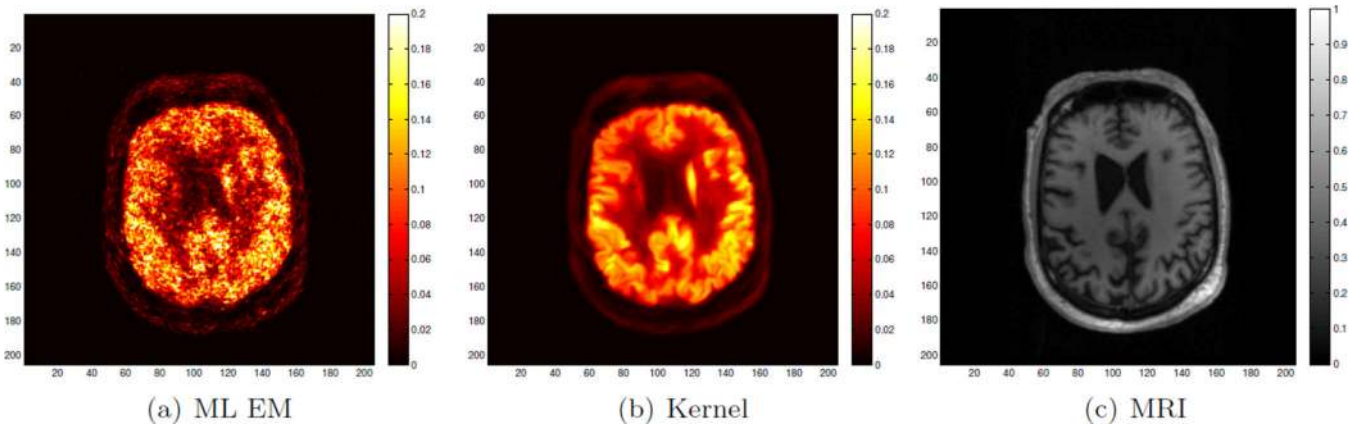

Figure 10.

A transaxial slice of the reconstructed patient images. (a) ML EM reconstruction with 50 iterations. (b) The kernel method with 40 neighbors from a 7 × 7 × 7 search window. (c) MR image of the same slice.

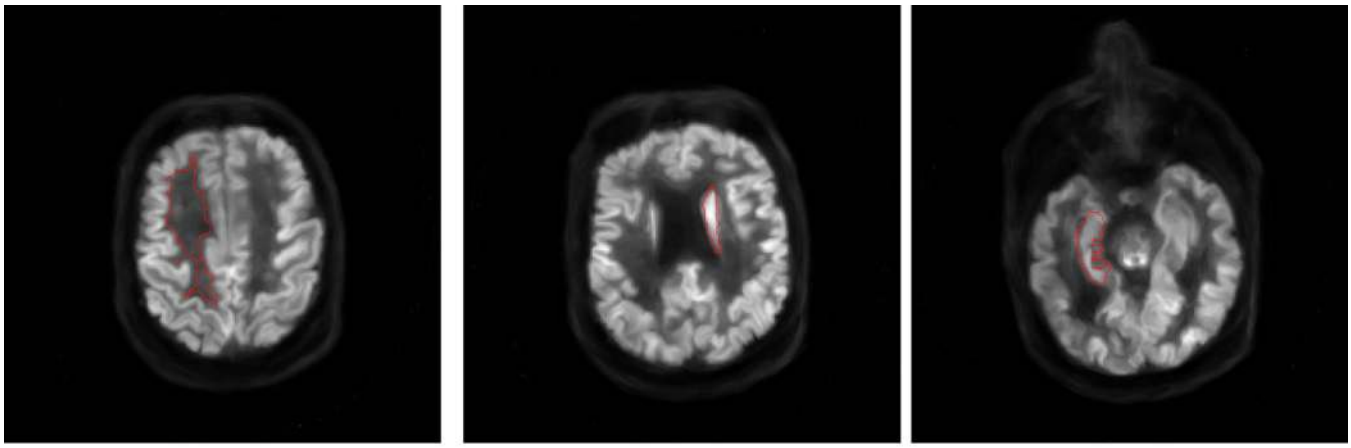

(a) white matter background (b) left caudate (c) right hippocampus

Figure 11.

Target and background regions used for quantification. The region edge, as determined from Freesurfer, is overlaid on the MRI image. In the case of the white matter background, the region was eroded to increase the separation between the background intensity and the uptake in surrounding structures. (a) white-matter background, (b) right caudate, (c) left hippocampus. All the regions are in 3D.

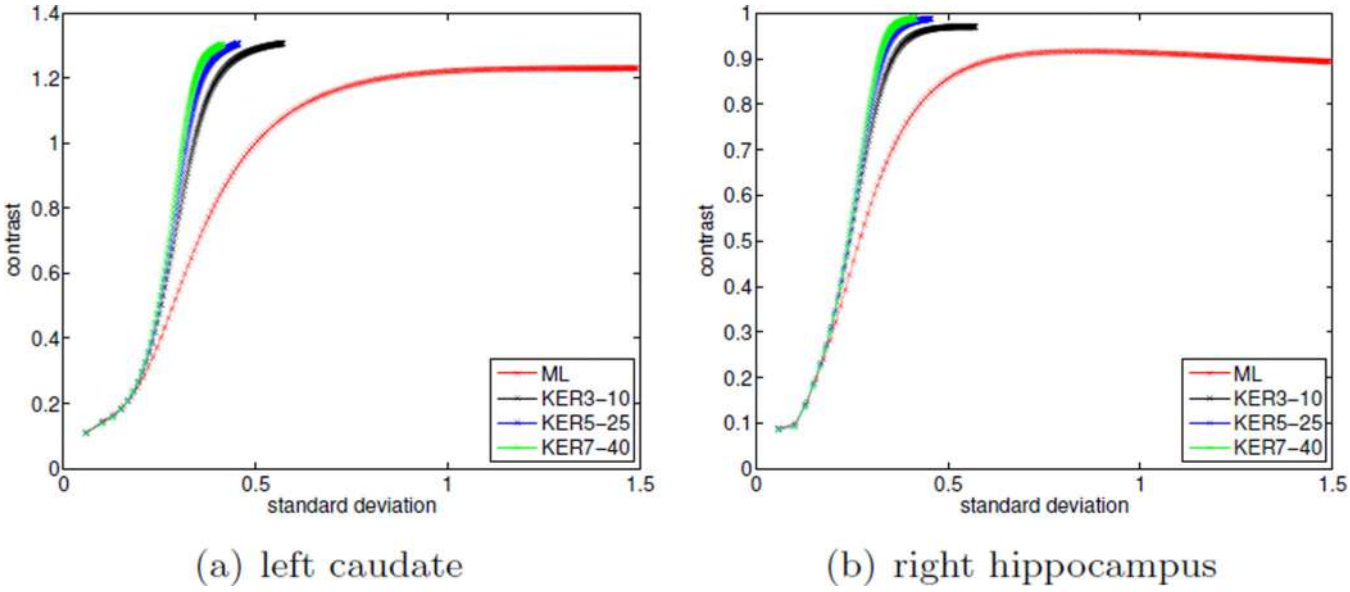

Figure 12.

Contrast vs. background noise curves for the ROIs in the patient images. (a) right caudate, (b) left hippocampus. In the legend, KER3-10 denotes a search window size of $3 \times 3 \times 3$ with 10 chosen neighbors.